Magnetic soft microfiberbots for robotic embolization

Xurui Liu[1, 2]†, Liu Wang[3, 4]†, Yuanzhuo Xiang[2]†, Fan Liao[1, 2], Na Li[1, 2], Jiyu Li[3], Jiaxin Wang[5], Qingyang Wu[1, 2], Cheng Zhou[1, 2], Youzhou Yang[1, 2], Yuanshi Kou[1, 2], Yueying Yang[1, 2], Hanchuan Tang[1, 2], Ning Zhou[6], Chidan Wan[7], Zhouping Yin[8, 9], Guang-Zhong Yang[10]*, Guangming Tao[2, 11, 12, 13]*, Jianfeng Zang[1, 2, 9]*

[1]School of Integrated Circuits, Huazhong University of Science and Technology, Wuhan 430074, China

[2]Wuhan National Laboratory for Optoelectronics, Huazhong University of Science and Technology, Wuhan 430074, China

[3]CAS Key Laboratory of Mechanical Behavior and Design of Materials, Department of Modern Mechanics, University of Science and Technology of China, Hefei 230026, PR China

[4]State Key Laboratory of Nonlinear Mechanics, Institute of Mechanics, Chinese Academy of Science, 15 Beisihuan West Road, Beijing 100190, China

[5]Department of Urology, Tongji Hospital, Tongji Medical College, Huazhong University of Science and Technology, Wuhan 430030, PR China.

[6]Division of Cardiology, Department of Internal Medicine, Tongji Hospital of Tongji Medical College of Huazhong University of Science and Technology, Wuhan 430074, China

[7]Department of Hepatobiliary Surgery, Union Hospital, Tongji Medical College, Huazhong University of Science and Technology, Wuhan 430074, China

[8]Flexible Electronics Research Center, State Key Laboratory of Digital Manufacturing Equipment and Technology, School of Mechanical Science and Engineering, Huazhong University of Science and Technology, Wuhan, Hubei 430074, China

[9]The State Key Laboratory of Intelligent Manufacturing Equipment and Technology, School of Mechanical Science and Engineering, Huazhong University of Science and Technology, Wuhan 430074, China

[10]Institute of Medical Robotics, Shanghai Jiao Tong University, Shanghai 200240, China

[11]The State Key Laboratory of Material Processing and Die & Mould Technology, School of Materials Science and Engineering, Huazhong University of Science and Technology, Wuhan, 430074 China

[12]Key Laboratory of Vascular Aging, Ministry of Education, Tongji Hospital, Tongji Medical College, Huazhong University of Science and Technology, Wuhan 430030, China

[13]Institute of Medical Equipment Science and Engineering, Huazhong University of Science and Technology, Wuhan 430074, China

†These authors contributed equally to this work.

*Corresponding authors. Email: gzyang@sjtu.edu.cn (G.-Z.Y.); tao@hust.edu.cn (G.T.); jfzang@hust.edu.cn (J.Z.)

*Corresponding authors. Email: gzyang@sjtu.edu.cn (G.-Z.Y.); tao@hust.edu.cn (G.T.); jfzang@hust.edu.cn (J.Z.);

This PDF file includes:

Supplementary text

Figs. S1 to S22

Table S1

References (*19-20, 23, 25, 28-30, 40, 53-56*)

Legends for Movies S1 to S14

Other Supplementary Materials for this manuscript include the following:

Movies S1 to S14

Supplementary Text

Analysis of the anchored state of microfiberbot in flow conditions.

The flow velocity distribution inside a cylindrical vessel can be expressed *(40,53,54)*

$$v_r = f(r, H)v_m \tag{6}$$

where H is the diameter of the vessel, r denotes the position with respect to the cylinder center O, and the mean flow velocity v_m. Considering that the diameter of the fiber (d = 60 μm) is much smaller than the vessel diameter (H = 800 μm), the position of the anchored microfiberbot can be estimated as

$$r = H/2 - d \tag{7}$$

In a flow condition with $v_m = 100$ mm/s and then gives the flow velocity at the microfiberbot

$$v_r = 15 \text{ mm/s} \tag{8}$$

Therefore, the fluidic drag force applied on one pitch of the microfiberbot can be estimated as

$$F_d = \frac{1}{2}\xi\rho S v_r^2 \tag{9}$$

where ξ is the drag coefficient, ρ is the flow density, S is the cross-section area of the microfiberbot. Substituting ξ = 0.15 *(55)*, $\rho = 1.11 \times 10^3$ kg/m^3, $S = 1.39 \times 10^{-7}$ m^2 into the equation, we obtain that $F_d = 2.61 \times 10^{-9}$ N. According to the FEA simulation results, the total contact friction $F_f = 2.03 * 10^{-6}$ N.

Table. S1. Comparison between this work and existing embolization procedure

Strategy		Target indication	Embolic agent type	Embolic agent deployment technique	Steerability (Max bifurcation angle θ, min diameter of accessible vessels H)	Maneuverability in flow conditions	Shape-morphing capability	Embolization Validation	Ref.
Commercial passive catheters		Aneurysm and tumor	Coil	Manually pushing/twisting guidewire to target lesions, followed by catheter delivery	Low $\theta < 90^\circ$ $H \sim 1$ mm	Intermediate (Buckled/looped in tortuous blood vessels)	Bending only	Commercial	**Catheter:** TERUMO Headway 27™ **Coil:** Stryker, Target™ Nano™
Active robots	Tethered hydraulic catheters	Aneurysm	Coil		Intermediate $\theta > 90^\circ$ $H \sim 2.5$ mm			In vivo (Porcine)	*19*
	Tethered electronic catheters	Aneurysm	Coil		Low $\theta > 90^\circ$ $H \sim 2.5$ mm			In vitro	*20*
	Tethered magnetic guidewire	Aneurysm	Coil		Intermediate $\theta > 90^\circ$ $H \sim 2.5$ mm			In vitro	*23*
	Tethered magnetic catheter	Tumor	Liquid embolic	Catheter-directed to blood vessel & passively carried by blood flow & passively aggregate at target lesions	Intermediate $\theta < 90^\circ$ $H \sim 100$ μm	Intermediate (Impractical in unpredictable flow conditions)		Ex vivo	*25*
	Flow-driven swarms	Tumor	Particle		High (Theoretically can steer to submillimetre regions due to the micro-size)	Low (Untraceable & passive drifted)	Particle aggregation	In vivo (Porcine)	*28*
	Flow-driven particles	Tumor	Particle					In vitro	*29*
	Flow-driven anchors	Tumor	Particle				Radial expansion	In vivo (Rabbit)	*30*
	Magnetic soft microfiberbots	**Aneurysm and tumor**	**Coil and particle**	**Catheter-directed to blood vessel & active navigation in blood flow & shape-morphing at target lesions**	**High** **$\theta > 90^\circ$** **$H \sim 100$ μm**	**High (Controlled by magnetic fields & visible to X-ray/ultrasound)**	**Elongation, contraction, aggregation**	**In vivo** (Rabbit)	**This work**

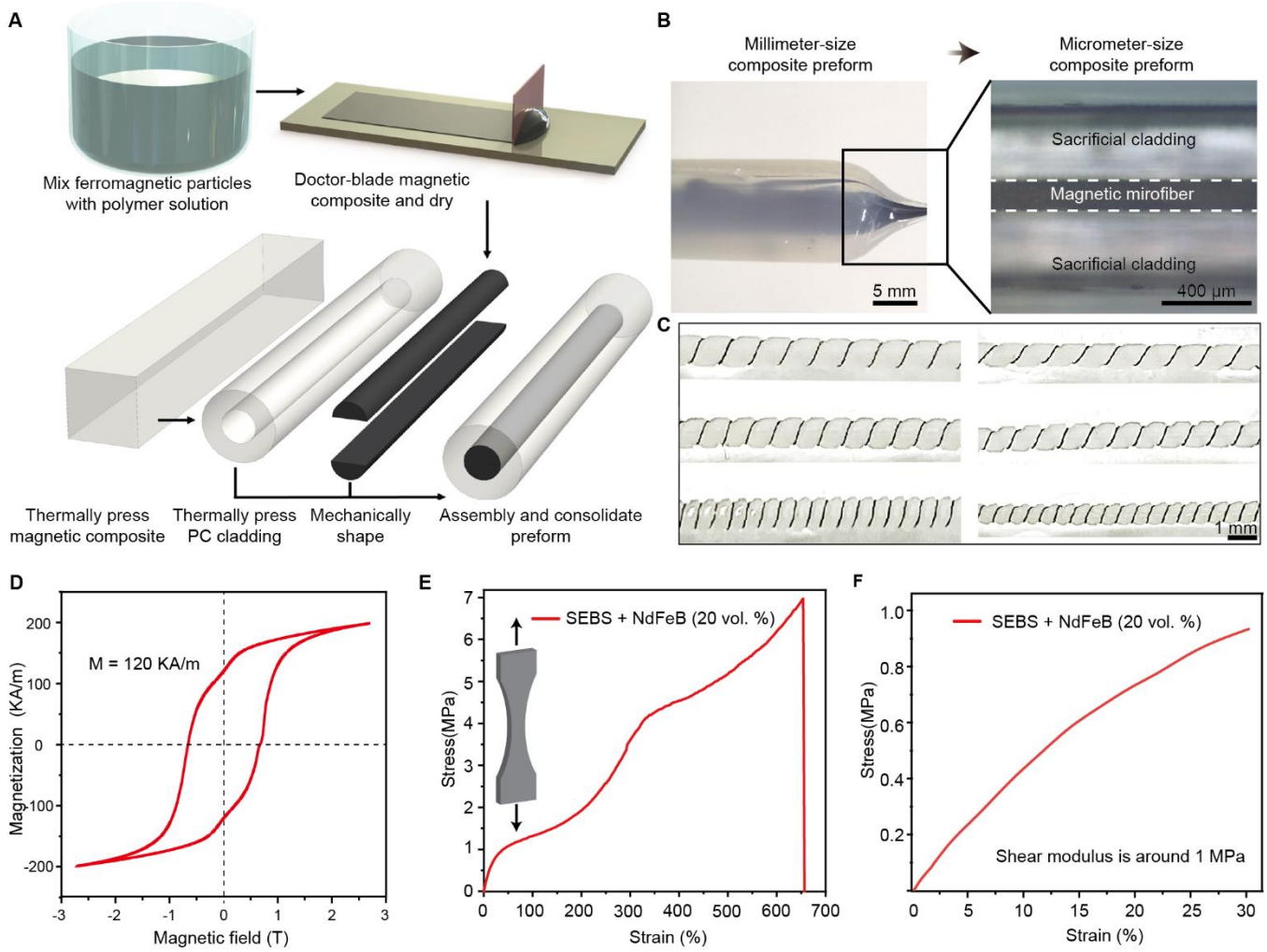

Fig. S1. Fabrication and characterization of magnetic soft microfiberbots. (A) Schematic of fabrication of millimeter-scale magnetic composite preform. **(B)** A millimeter-scale preform is thermally drawn into a micrometer-size fiber with sacrificial PC cladding and magnetic microfiber core. **(C)** the magnetic fiber can be molded into magnetic soft microfiberbots with identified helical geometry parameters by employing different molds. **(D)** Magnetic hysteresis of SEBS+NdFeB (20 vol.%) composite. Residual magnetization **M**=120 kA/m. **(E)** Stress-strain curves of SEBS+NdFeB (20 vol.%) composite. **(F)** Fitting the stress-strain curve by the incompressible neo-Hookean constitutive model (Shear modulus is around 1 MPa).

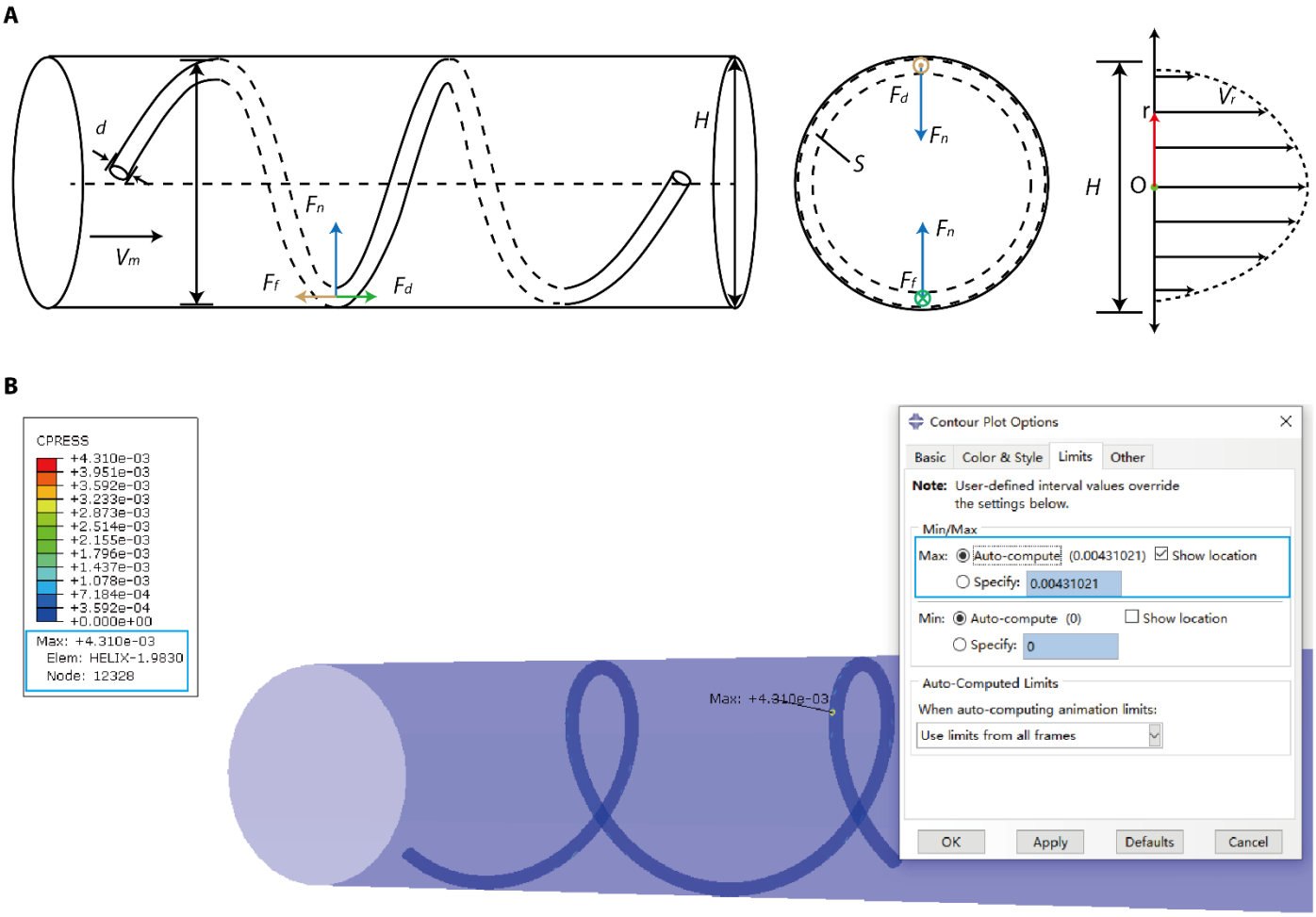

Fig. S2. Analysis of the anchored state of microfiberbot in flow conditions. (A) The fluidic drag force (per pitch) F_d is estimated by the drag pressure times the cross-sectional area of the microfiberbot ($S = \pi\left(\frac{H^2}{4} - \left(\frac{H}{2} - d\right)^2\right)$). **(B)** FEA simulations analyze the contact pressure between microfiberbots and the vessel wall.

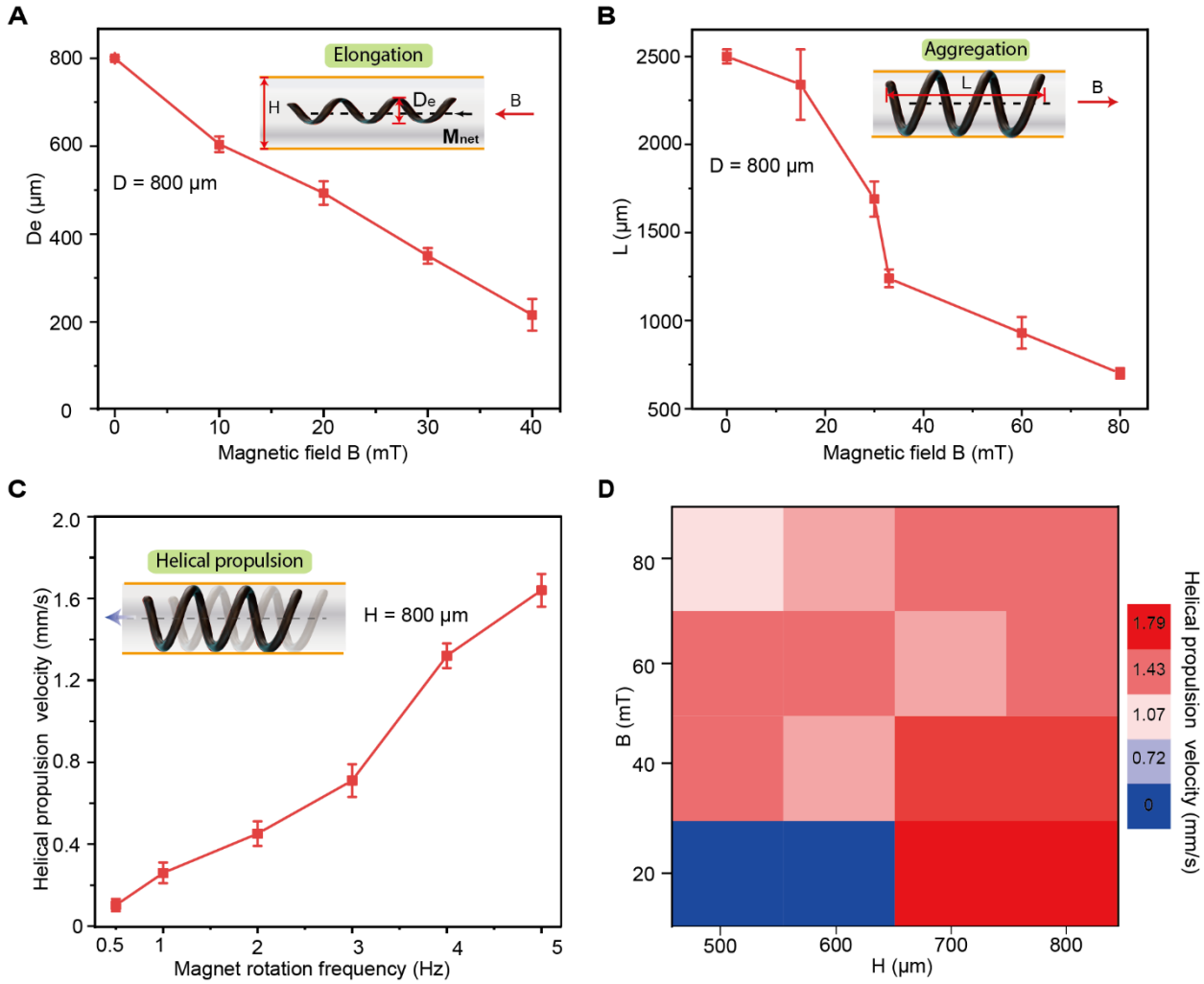

Fig. S3. Characterization of microfiberbots with helical diameter of 800 μm under varying magnetic parameters. (A) Helical diameter of microfiberbot as a function of actuation magnetic field strength. **(B)** Length of the microfiberbot as a function of actuation magnetic field strength. **(C)** Helical propulsion velocity as a function of magnet rotation frequency in the absence of flow (B = 40 mT). **(D)** Helical propulsion velocity within vessels with different diameters H (Each experiment was conducted three times, $N = 3$).

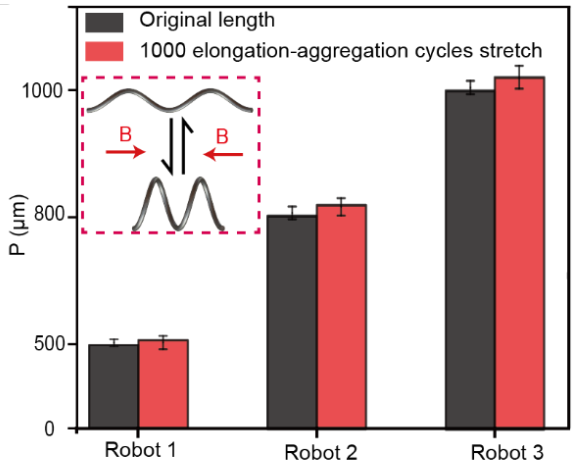

Fig. S4. Reversibility test of the shape morphing of the microfiberbot. After 1000 elongation-contraction cycles, the pitch of the four magnetic soft microfiberbots (Pitch p = 500, 800, and 1000 μm) remains almost unchanged (Each experiment was conducted three times, N = 3).

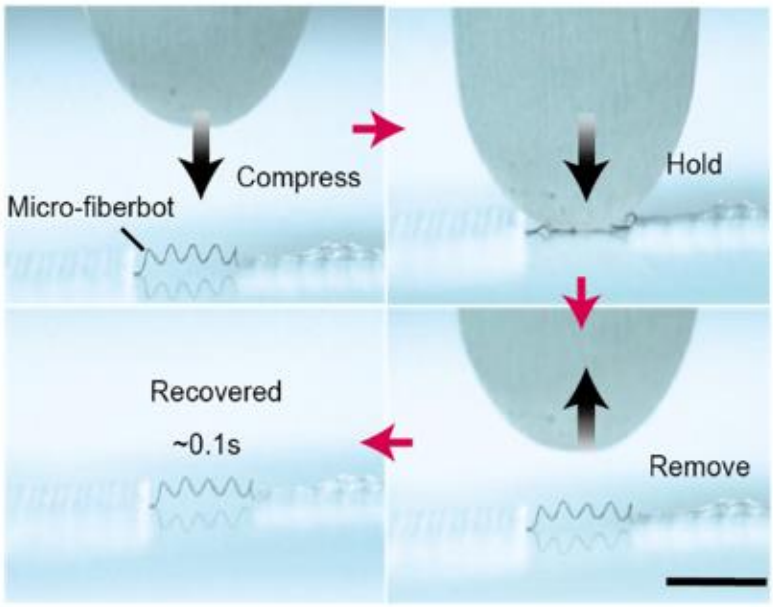

Fig. S5. High elasticity and mechanical robustness of the microfiberbot. The magnetic soft microfiberbot quickly (0.1 s) recovers to the initial helical shape after being compressed by a rigid punch. Scale bar, 5 mm.

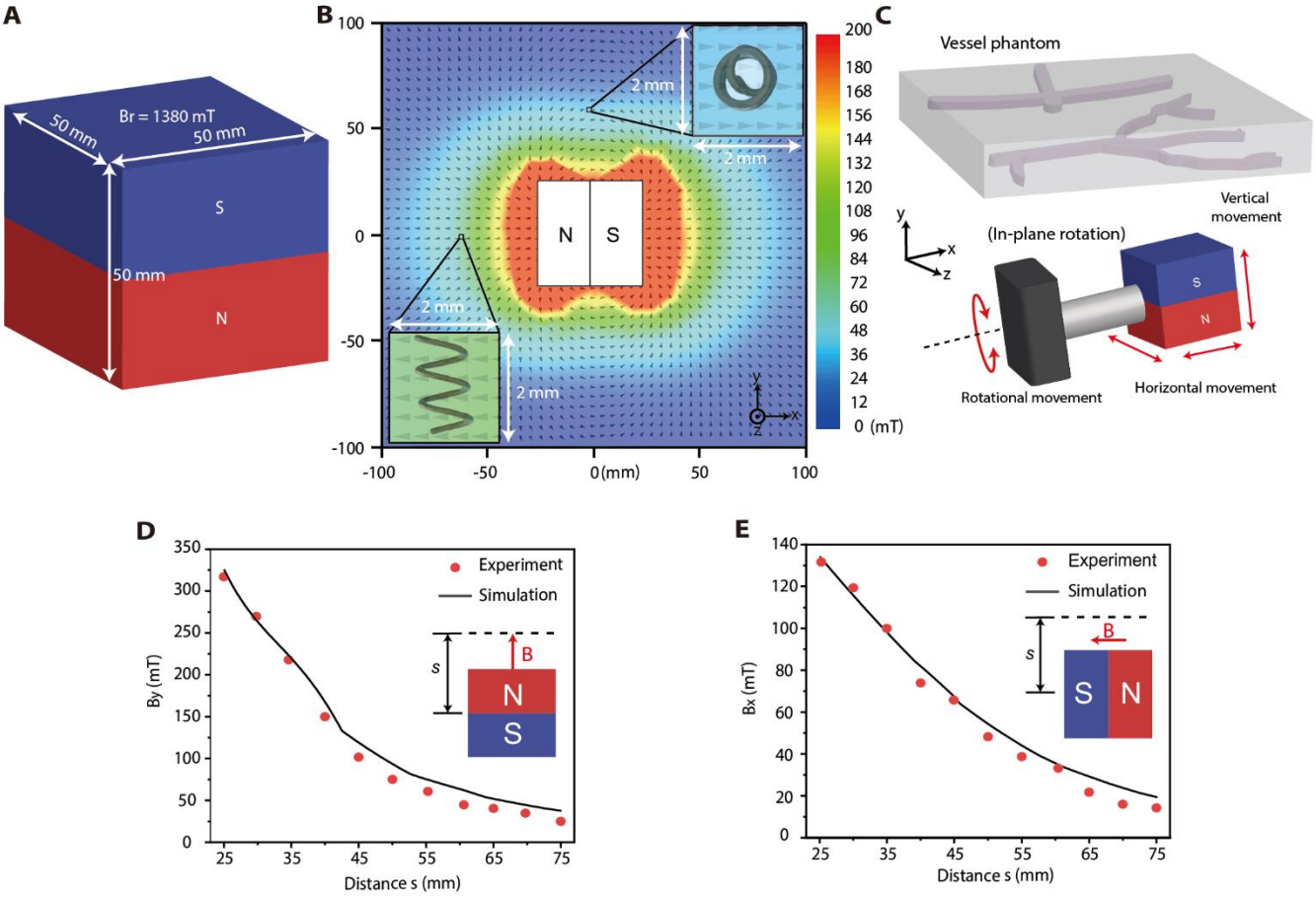

Fig. S6. Control strategy of microfiberbots using a cubic magnet. (A) Schematic of the cubic magnet with a residual magnetic flux density $\mathbf{B_r}$ =1380 mT. **(B)**The magnetic fields around the cubic magnet. **(C)** The magnetic actuation for microfiberbot is achieved by dynamically controlling the vertical, horizontal, and rotational movements of the cube magnet. **(D)** The magnetic field strength B_x as a function of distance *s* along the centerline of the magnet. **(E)**The magnetic field strength B_y as a function of distance *s* along the centerline of the magnet.

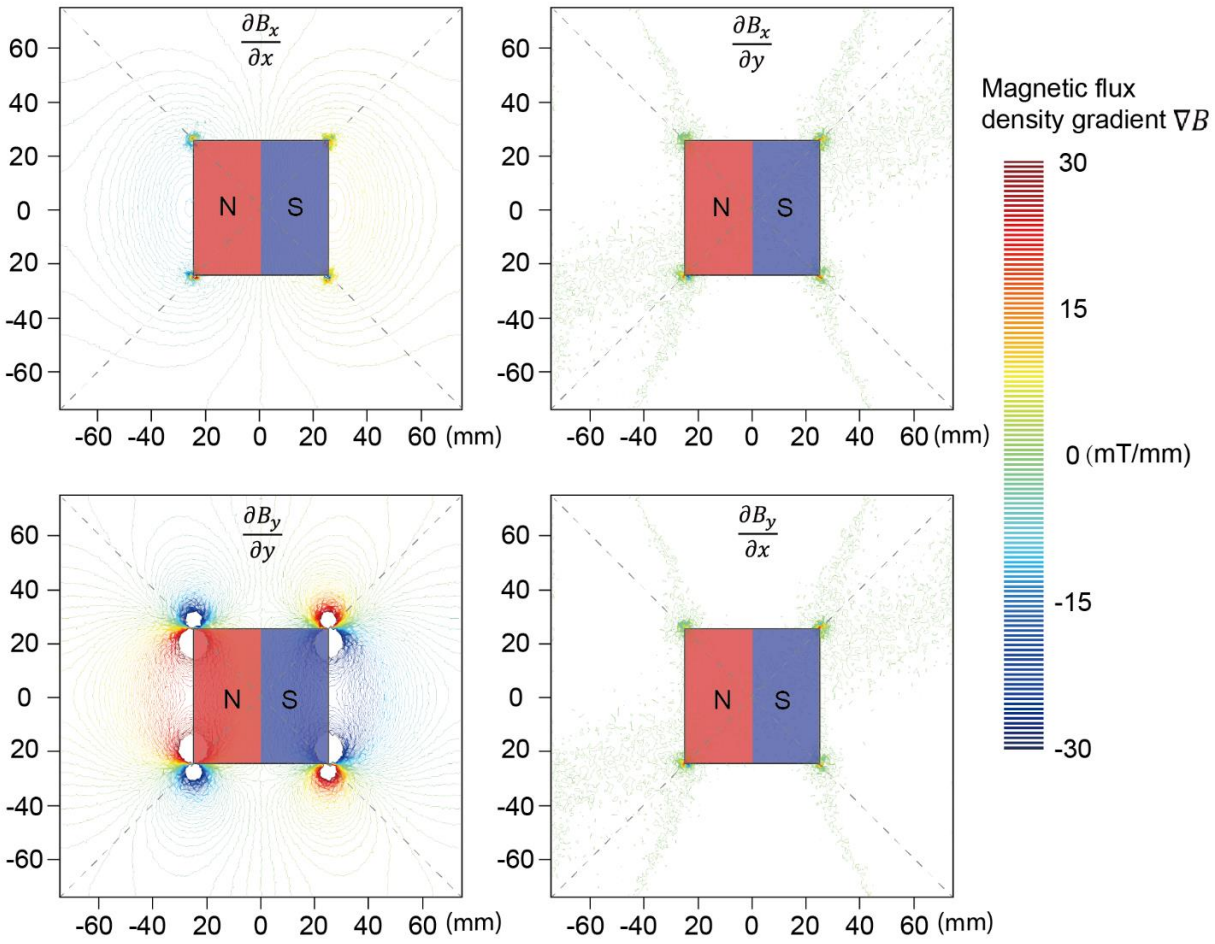

Fig. S7. Spatial magnetic gradient distribution of a cubic magnet with a width of 50 mm.

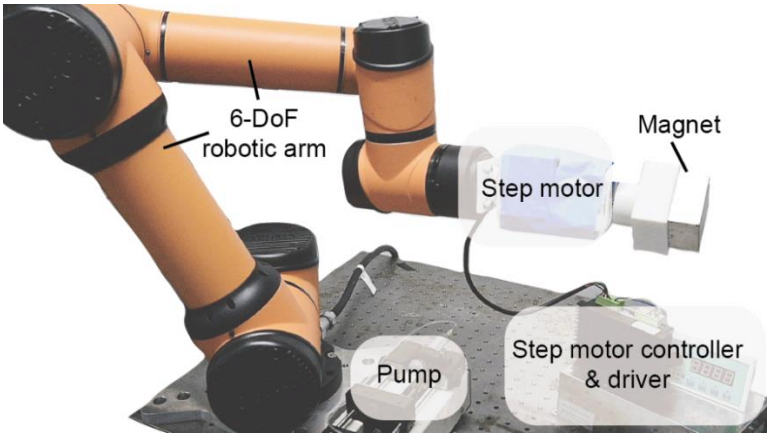

Fig. S8. Magnetic maneuvering system. The magnetic maneuvering system is composed of 6-DoF robotic arm, a step motor controller and driver, and a cubic magnet.

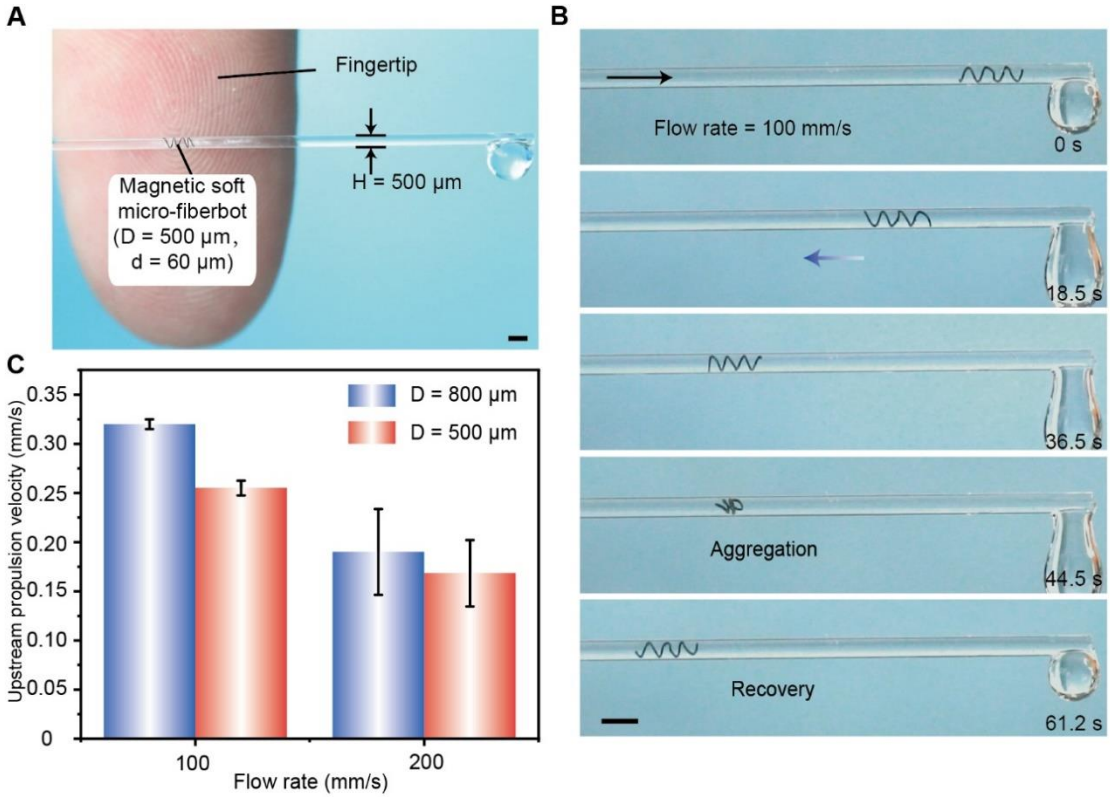

Fig. S9. Demonstration of shape-morphing capability and in-flow maneuverability of microfiberbot with 500 μm diameter. (A) Image of a microfiberbot inside a tube with a 500 μm diameter. **(B)** The 500 μm microfiberbot can still have shape-morphing and upstream propulsion in a flow condition with 100 mm/s flow rate. Scale bar, 1 mm. **(C)** The upstream propulsion velocity of the 500 μm robot is comparable to that of the 800 μm microfiberbot in both 100 mm/s and 200 mm/s flow (Each experiment was conducted three times, $N = 3$).

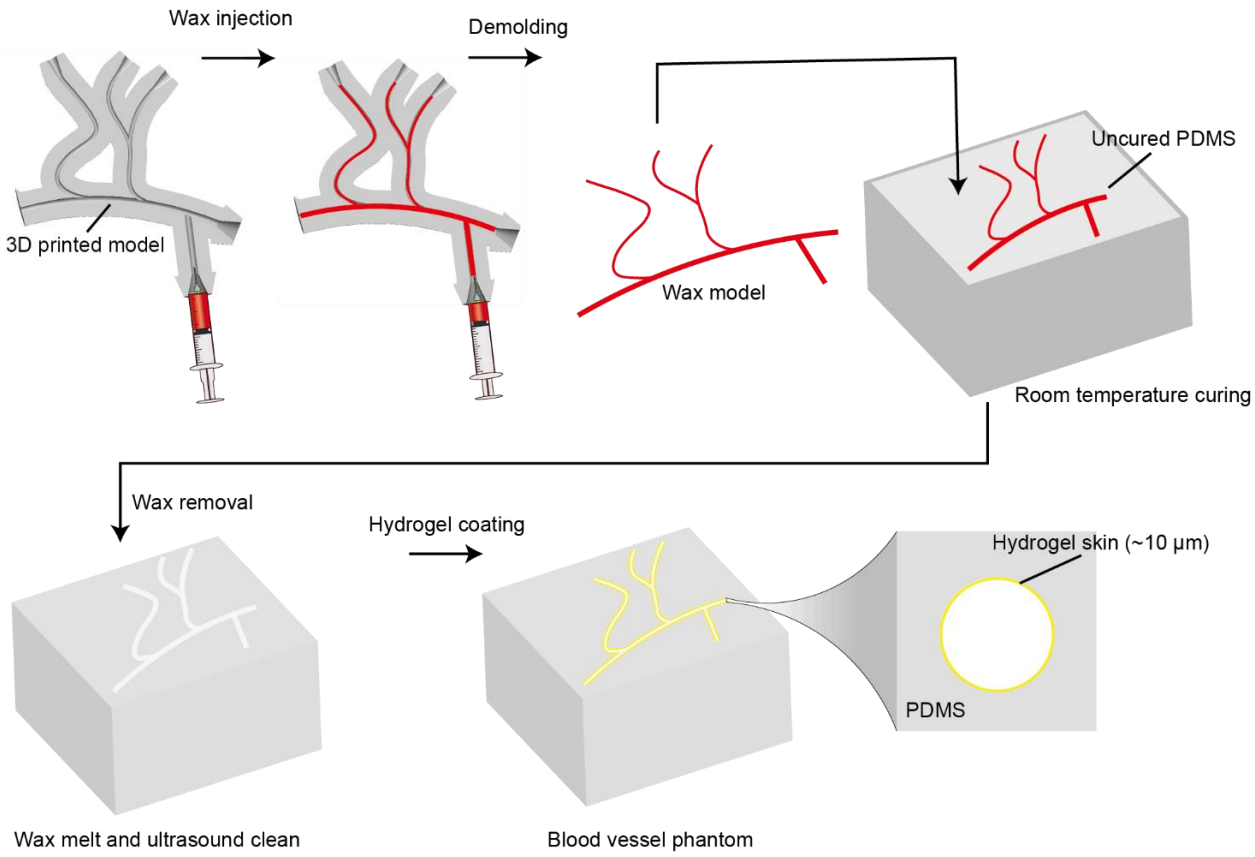

Fig. S10. Fabrication of blood vessel phantoms. The sacrificial template method was used to fabricate the vessel phantom. Melted wax was first injected into 3D-printed negative molds, and then solidified wax mold with the desired shape was carefully taken out. Next, the wax mold was immersed into uncured PDMS (mass ratio 10:1) and cured at room temperature (23℃) for 72 hours. Lastly, the phantoms were placed on a hot plate (120℃) to melt the wax and the vessel phantom with hollow lumen structure was placed in ultrasound cleaner with ethanol for 2 h. To obtain similar friction conditions to realistic blood vessels, a thin hydrogel layer (10 μm) was coated in the inner surface of the hollow lumen structure *(56)*. Therefore, the vessel phantoms have similar Young's modulus properties (2 MPa) and friction properties with the coefficient of 0.1.

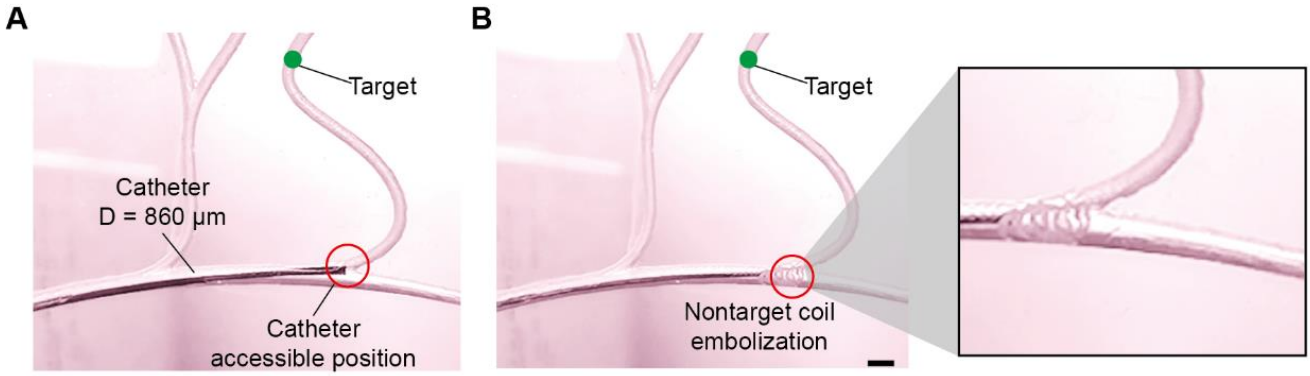

Fig. S11. Demonstration of nontarget coil embolization using a commercial catheter. (A) Commercial catheter can only reach the second bifurcation. **(B)** The limited accessibility of catheter may lead to nontarget coil embolization. Scale bar, 2 mm.

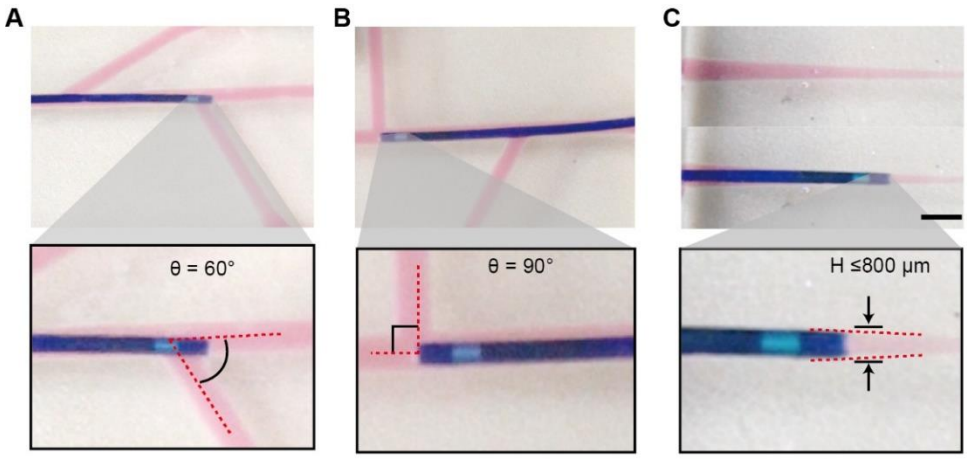

Fig. S12. Demonstration of the low steerability of a commercial catheter. (A-B), The commercial catheter cannot be steered to the bifurcation vascular phantom with bifurcation angle (A) θ = 60° and (B) 90°. **(C)** The commercial catheter cannot access narrowing branches with diameter smaller than its tip. Scale bar, 2 mm.

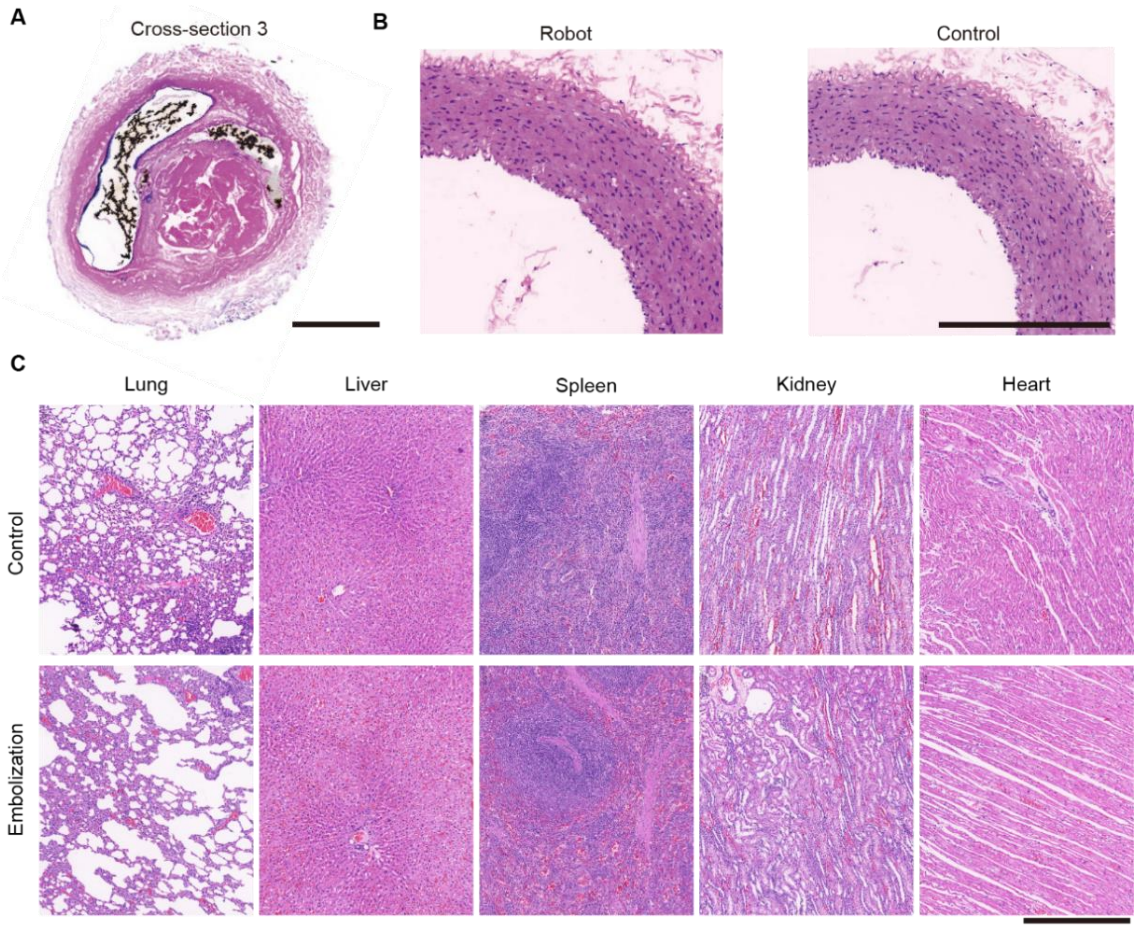

Fig. S13. Histology analysis of main organs of rabbits after three-week embolization surgery. (A) The cross-section 3 of H&E staining cross-section images were selected from the proximal to distal blood vessels to validate the embolization results. Scale bar, 250 μm. **(B)** The hematoxylin and eosin (H&E) staining cross-section image of the rabbit femoral artery. The sample for the soft microfiberbot group was collected after locomotion. Scale bar, 250 μm. **(C)** No inflammation or pathological abnormalities were observed in the samples collected from the control group and embolization group of rabbits. Scale bar, 500 μm.

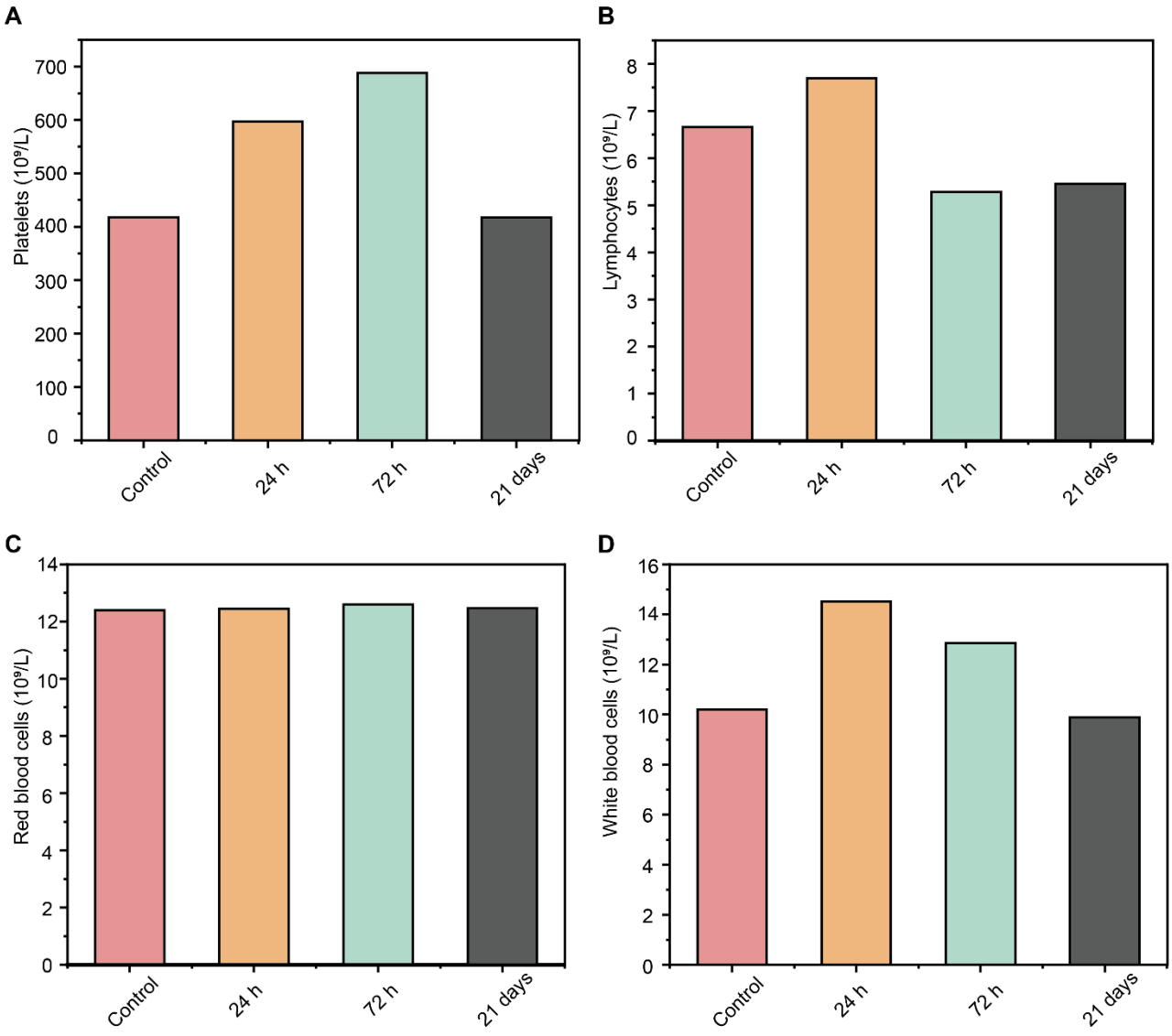

Fig. S14. Comprehensive blood cell counts taken from a rabbit before and after embolization (24 h, 72 h, 21 days).

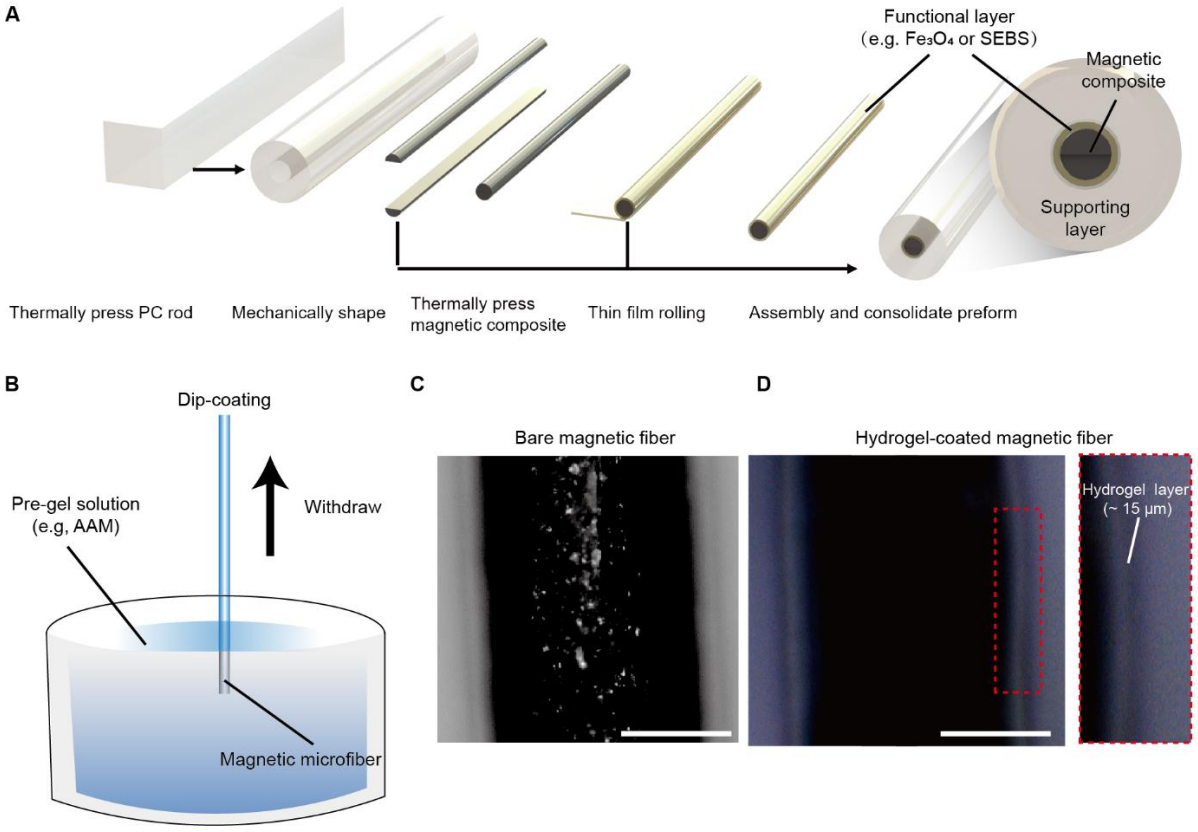

Fig. S15. Fabrication of coating hydrogel skin. (A) Schematic of the steps used to fabricate millimeter-scale magnetic composite preform with embedded functional layers. **(B)** Schematic of dip-coating hydrogel on a magnetic fiber in pre-gel solution (AAM). **(C)** The optical imaging of bare magnetic fiber shows that the magnetic particles are exposed without hydrogel coating. **(D)**After hydrogel coating, the magnetic particles were isolated and a hydrogel layer (15 μm) was observed. Scale bar 50 μm.

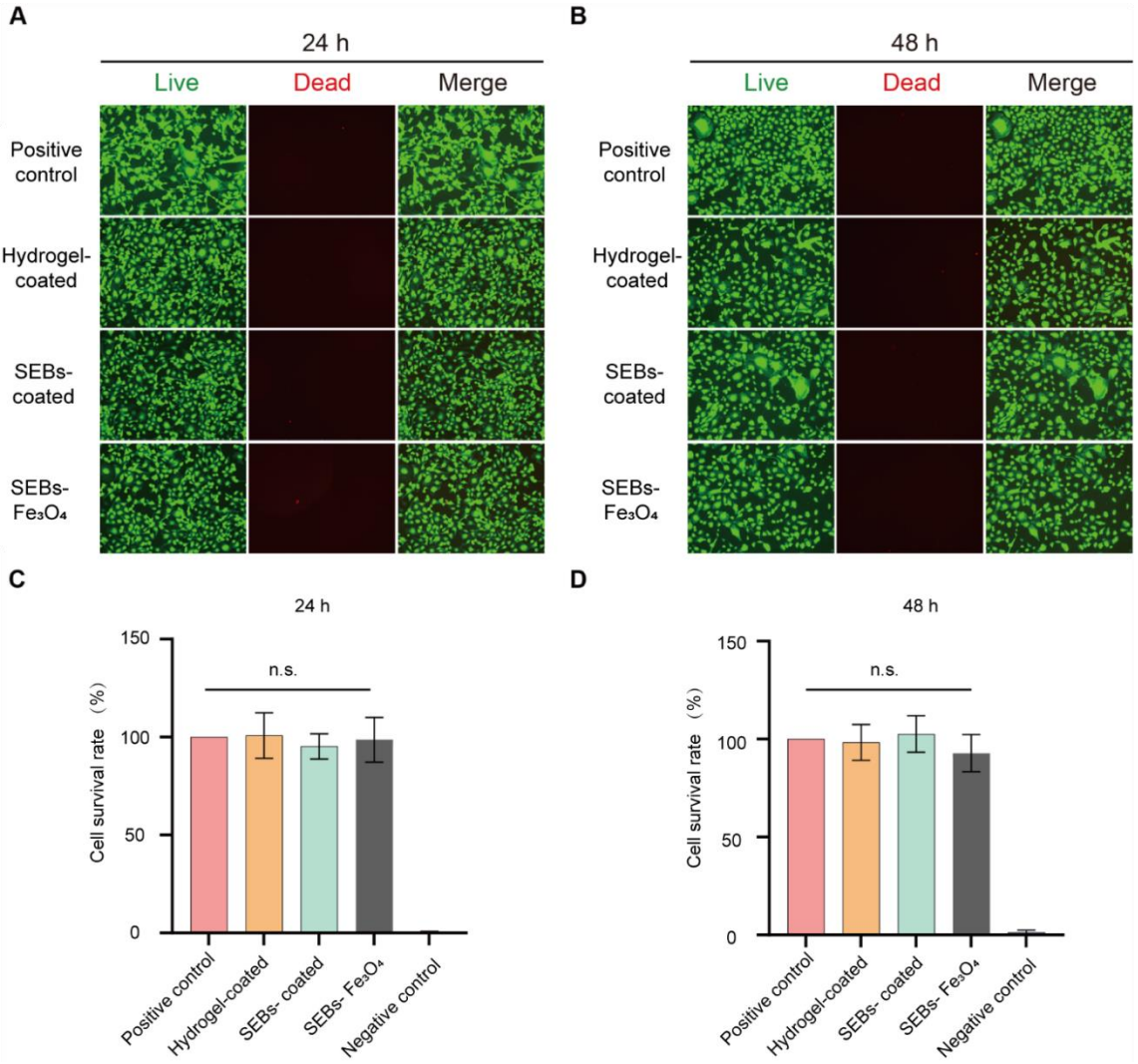

Fig. S16. Cell viability tests of magnetic composites with different coatings. (A) 24-hour exposure: Fluorescence microscopic images of human cardiac microvascular endothelial cells incubated with composites. **(B)** 48-hour exposure. **(C) and (D)** Relative cell survival rates for positive control, hydrogel-coated, SEBS-coated, and SEBS-Fe_3O_4 magnetic soft microfiberbots. (Each experiment was conducted three times, $N = 3$).

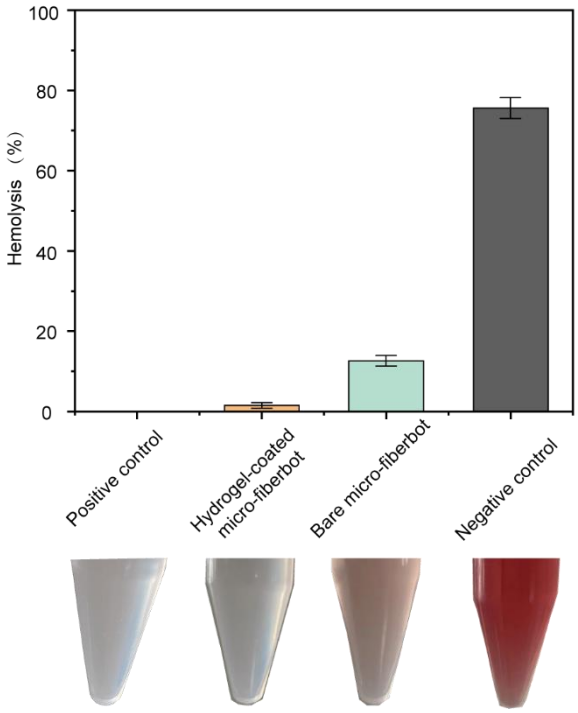

Fig. S17. Analysis of blood cell hemolysis of positive control, negative control, bare microfiberbots and hydrogel-coated microfiberbots (Each experiment was conducted three times, $N = 3$).

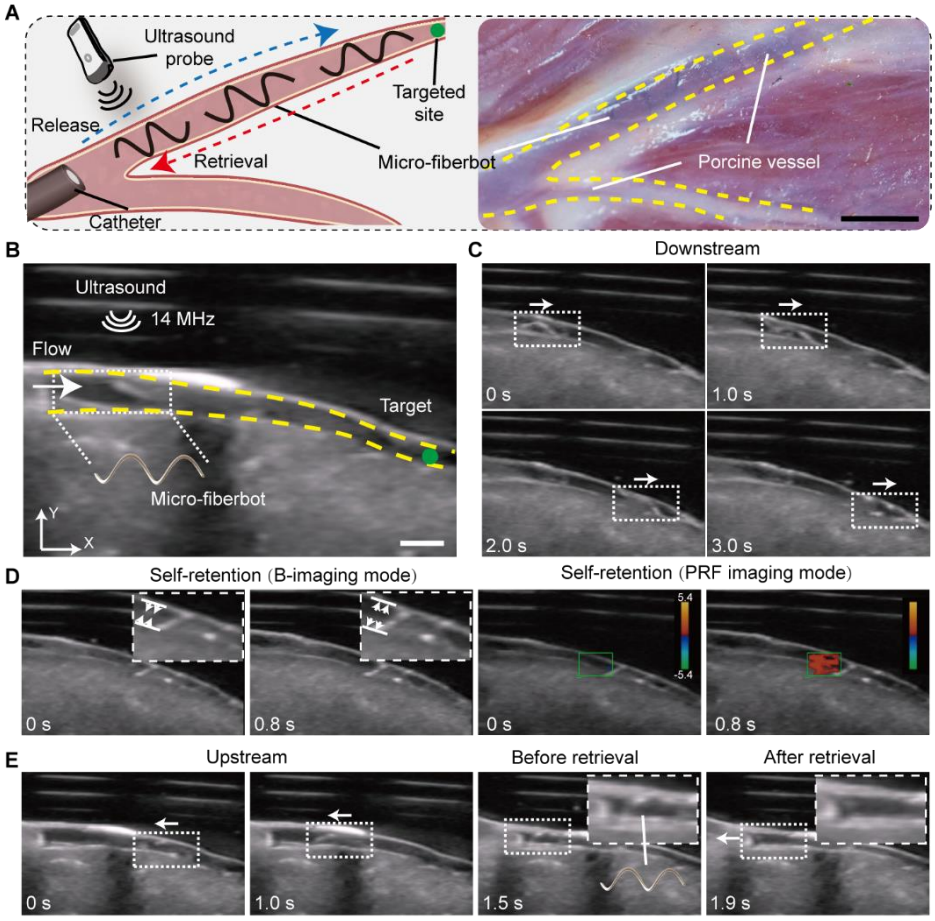

Fig. S18. Ex vivo demonstration of real-time ultrasound tracking capability of microfiberbots. (A) Schematic of magnetic soft microfiberbots locomotion and retrieval for targeted drug delivery under real-time ultrasound imaging. Right: The optical images of magnetic soft microfiberbots navigating in a porcine coronary artery. Scale bar, 5 mm. **(B)** Real-time ultrasound imaging-tracked navigation of magnetic soft microfiberbots controlled by the external magnetic manipulation system in an ex vivo porcine coronary artery under the flow. The white arrow indicates the flow directions. Scale bar, 2 mm. **(C)** Downstream navigation of magnetic soft microfiberbots to a targeted site. Red arrows show the navigation directions. **(D)** Magnetic soft microfiberbots self-retained in flow environments with dynamically changed porcine coronary artery diameters, the insets show the enlarged images of the magnetic soft microfiberbots. PRF: 1.0 kHz. **(E)** Upstream navigation and catheter retrieval of magnetic soft microfiberbots.

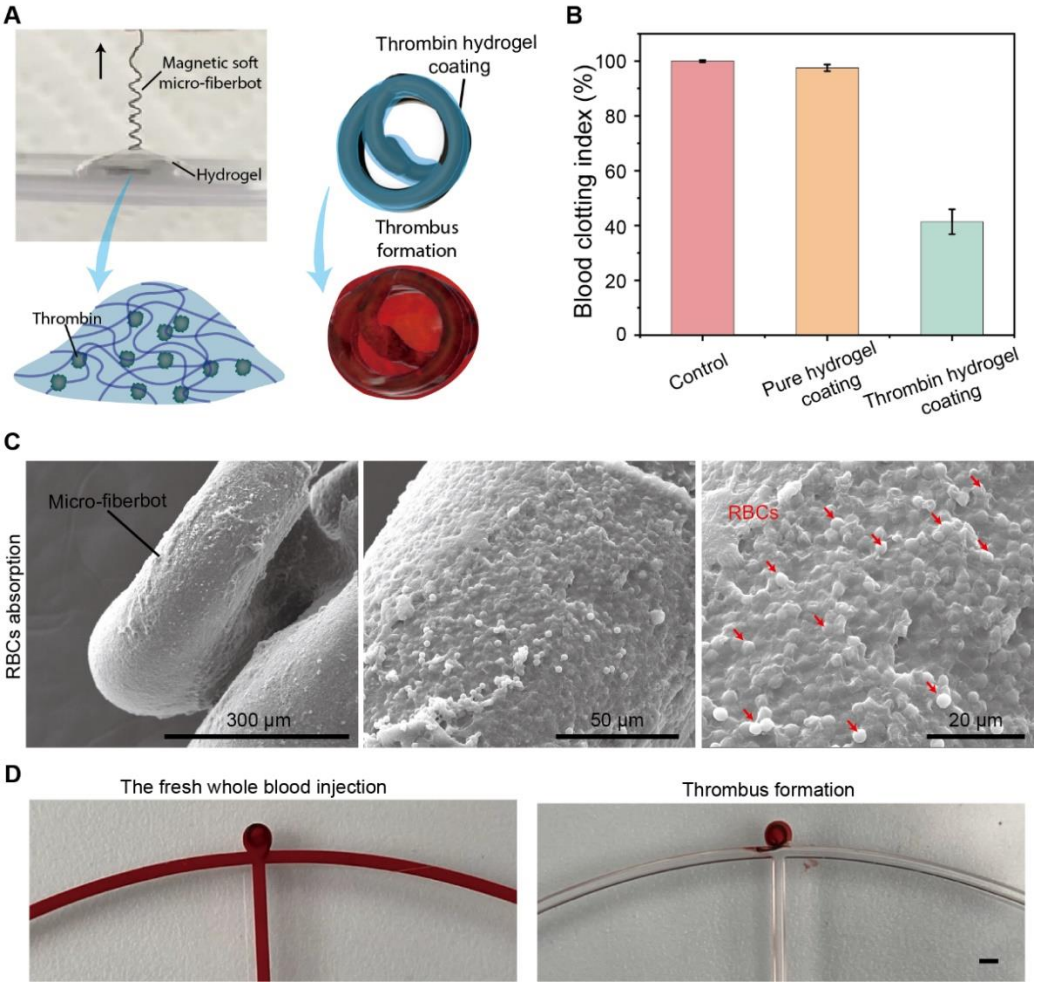

Fig. S19. Thrombin-hydrogel coating of the microfiberbot promotes thrombus formation. (A) Experimental image demonstrating the dip coating method used to form a thin layer of thrombin-hydrogel on the microfiberbot. **(B)** Blood clotting index of control, pure hydrogel coating, and thrombin-hydrogel coating groups (Each experiment was conducted three times, $N = 3$). **(C)** Scanning electron microscope (SEM) image displaying red blood cell (RBC) absorption on the microfiberbot. **(D)** Injection of blood to stimulate thrombus formation within the aneurysm phantom. Scale bar, 1 mm.

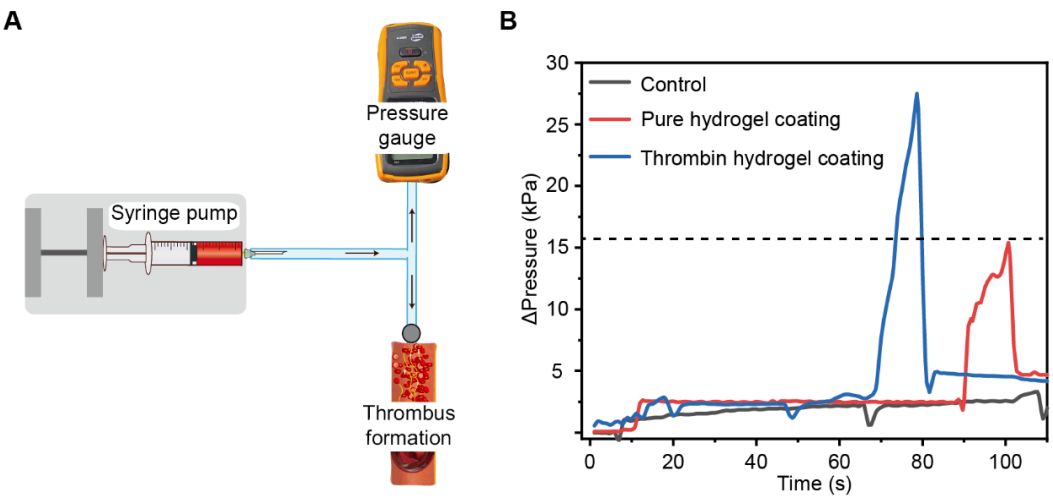

Fig. S20. Pressure assessment of the microfiberbot within a vessel phantom. (A) Schematic of the in vitro occlusion setup employing a syringe pump and a pressure gauge to measure the pressure needed to drive blood through the tube. **(B)** Pressure as a function of time for control (blood alone), pure hydrogel coating, and thrombin hydrogel coating.

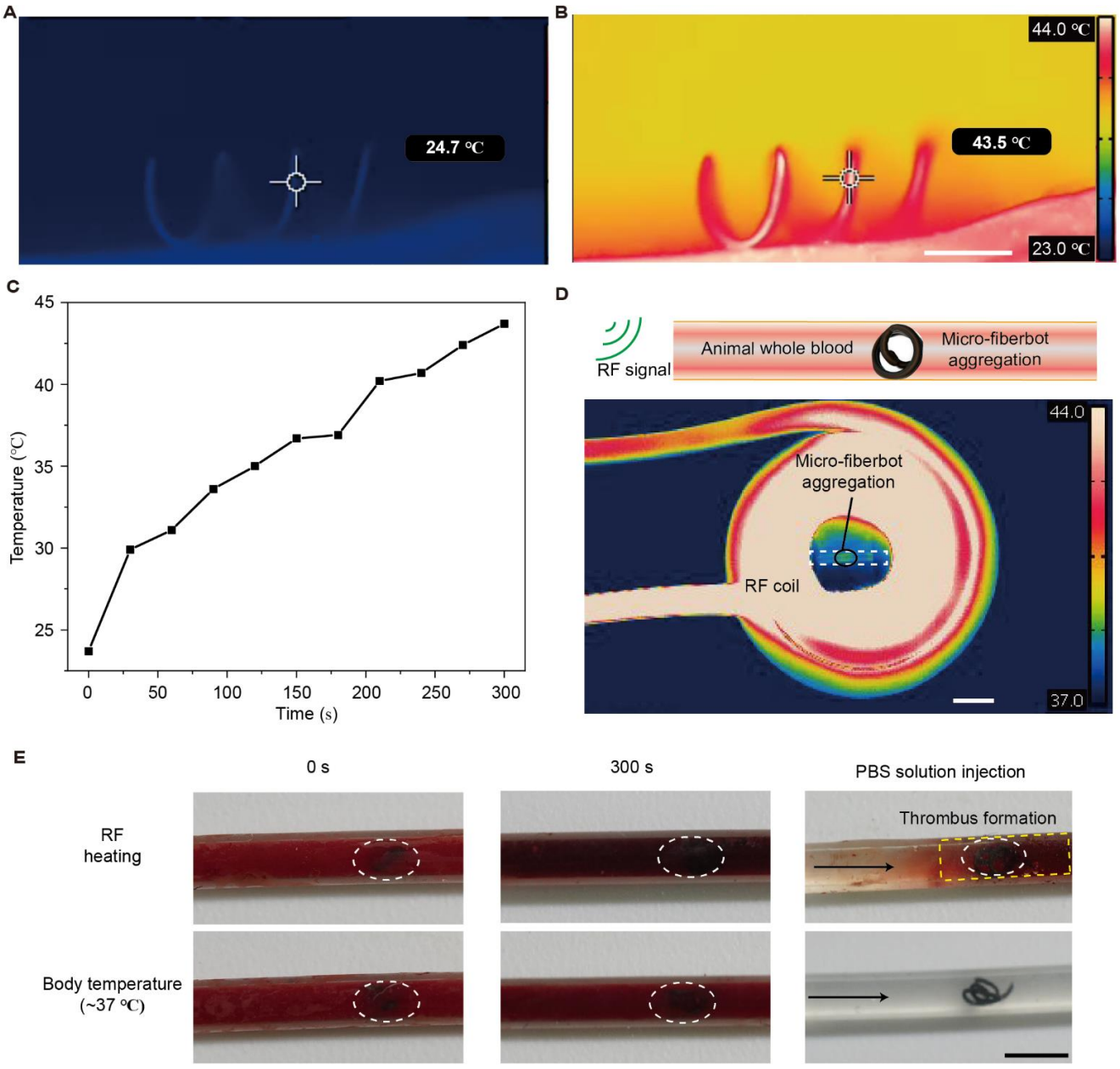

Fig. S21. Demonstration of microfiberbot under RF signal for local hyperthermia and thrombus formation. (A) Infrared picture shows the temperature of microfiberbots before RF heating. **(B)** Infrared picture shows the temperature of microfiberbots after RF heating. Scale bar, 1 mm. **(C)** The temperature change of microfiberbot in 300 seconds. **(D)** Microfiberbot was placed on the vessel phantom with animal whole blood and then heated by RF coil. Scale bar, 2 mm. **(E)** After 5 min RF heating, the thrombus formation was observed. As a comparison, without RF heating, no significant thrombus formation. Scale bar, 2 mm.

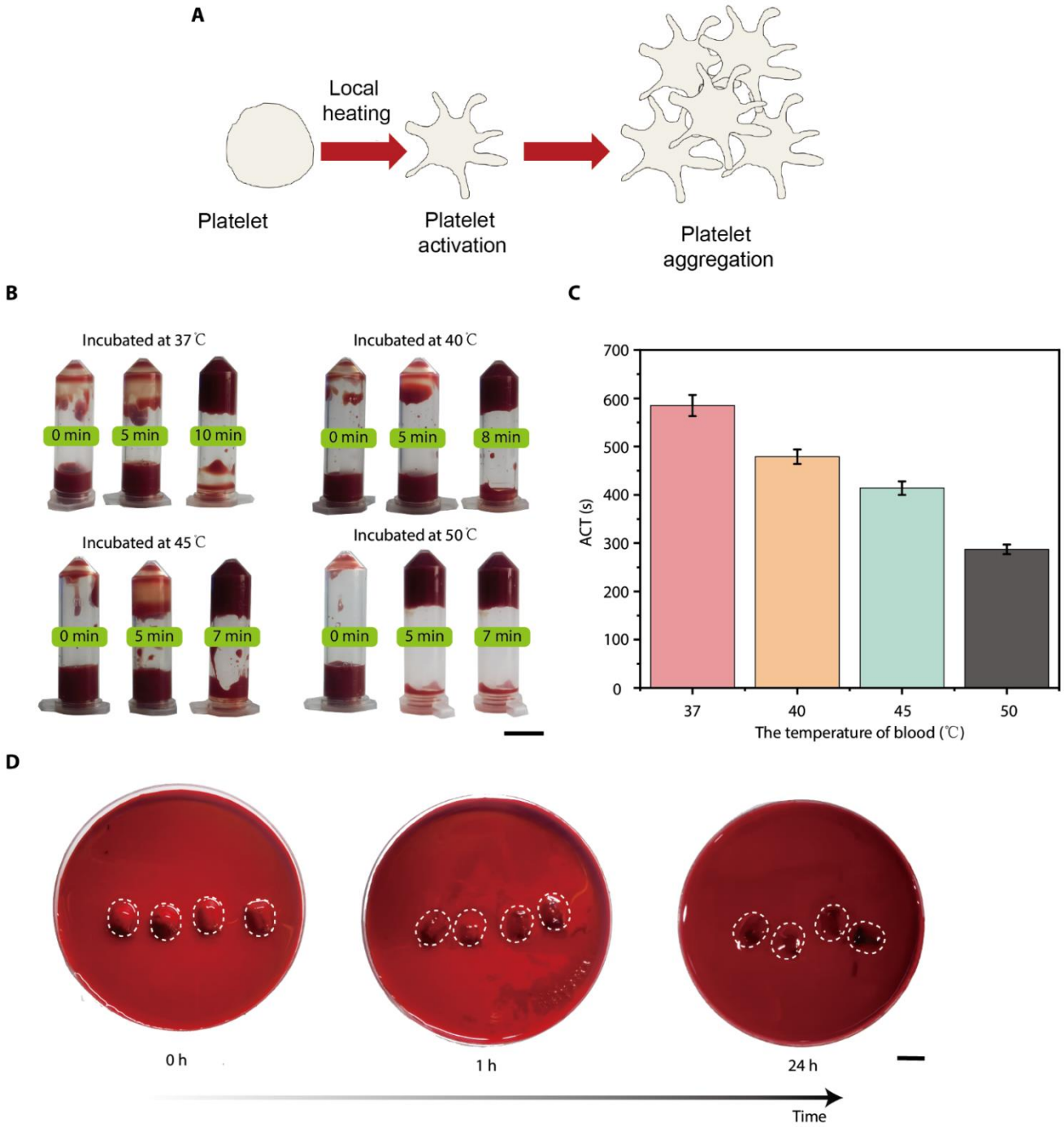

Fig. S22. Thrombus formation when incubated in different temperatures. (A) Schematic illustration of platelet activation and aggregation. **(B)** Images show the porcine whole blood incubated in four feature Temperature with different times. **(C)** Activated coagulation time (ACT) at different incubated temperatures (Each experiment was conducted three times, $N = 3$). **(D)** Temporal shape variation of formed thrombus in anticoagulated porcine blood. All scale bar, 10 mm.

Legends for Movies S1 to S14

Movie S1. Overview movie of magnetic soft microfiberbots for robotic embolization.
Movie S2. Shape morphing capability of microfiberbots under magnetic fields.
Movie S3. Magnetic maneuvering of microfiberbots in flow condition.
Movie S4 Demonstration of shape-morphing capability and in-flow maneuverability of microfiberbots with 500 μm diameter.
Movie S5. Catheter-assisted deployment of microfiberbots.
Movie S6. Demonstration of microfiberbots steering in bifurcation branches of blood vessel phantom.
Movie S7. Demonstration of microfiberbots steering in a narrowing blood vessel phantom.
Movie S8. Demonstration of microfiberbots steering in an S-shaped blood vessel phantom.
Movie S9. Demonstration of microfiberbots steering in a 3D blood vessel phantom.
Movie S10. In vitro demonstration of aneurysm embolization.
Movie S11. In vitro demonstration of tumor coil embolization.
Movie S12. In vitro demonstration of particle embolization protection and retrieval.
Movie S13. Robotic embolization with multiple microfiberbots.
Movie S14. In vivo demonstration of robotic embolization in a rabbit.